

# Application of variational and FEM methods to the modelling and numerical analysis of guillotining process for geometrical and physical nonlinearity

L. Bohdal\*, L. Kukielka\*\*

\*Koszalin University of Technology, Raclawicka str. 15-17, 75-638, Koszalin, Poland, E-mail: Bohdall@interia.pl

\*\*Koszalin University of Technology, Raclawicka str. 15-17, 75-638, Koszalin, Poland,  
E-mail: leon.kukielka@tu.koszalin.pl

**crossref** <http://dx.doi.org/10.5755/j01.mech.20.2.6941>

## 1. Introduction

Guillotining is a basic operation in the technological process of fabricating sheet metal parts. This process is used widely in industry (for primary metal and in the aerospace, automotive and construction industries) to produce long, straight sheet metal cuts. Two straight knives perform a shearing operation (Fig. 1). The upper knife is inclined and moves downwards at a set velocity, while the lower knife is fixed, and the sheet is clamped to the lower knife by a blank holder. When the upper knife is forced downwards, the sheet is progressively cut from one end to the other.

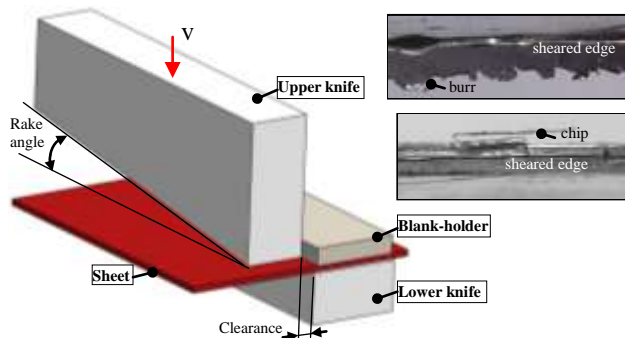


Fig. 1 Schematic of the guillotining process and typical defects in the sheet's sheared edge

The quality of the part after guillotining depends on many process parameters, such as the clearance between the knives in the horizontal direction, lubrication method, shearing velocity, knife geometry and method of clamping the sheet metal plates [1-3]. These parameters are key factors affecting energy consumption and physical phenomena occurring in the cutting process, such as the state of the material displacement, visco-plastic strain and stress. In turn, certain physical phenomena affect the material's mechanisms of separation in the cutting zone, such as visco-plastic shear or rupture, because the mechanism of the separation process depends on the quality of both the sheared edge and the product. There is currently no mathematical formula or methodology to allow for the proper selection of technological parameters. Therefore, the product frequently has serious defects and drawbacks, such as large deformation, twisting, bowing and defects on the sheared edge, such as burrs and chips (Fig. 1). Further processing, such as grinding, is required to eliminate the chips and burr formations, but it increases the production cost and time. Knowledge of the guil-

lotining process is based mainly on experimental methods, which are often expensive and unable to be extrapolated to other cutting configurations. Therefore, computational models, such as the finite element method (FEM), are valuable in reducing the number of trial-and-error experiments required to predict the state of material displacement, residual stresses, strains, material fracture, sheet deformations and quality of the sheared edge.

Only a few papers exist in the literature that demonstrate the modelling of the guillotining process using FEM. Wisselink and Hu'etink [4, 5] developed a finite element model of guillotining to calculate the steady state of such a process using the Arbitrary Lagrangian Eulerian formulation. An isotropic plastic constitutive equation combined with a simple uncoupled damage model was used to describe the material's behaviour. This model was based on stress triaxiality, which is defined as the ratio of the hydrostatic stress to the equivalent stress. The applicability of the material model was limited to relatively low shearing speeds ( $v = 1$  mm/s), however. The simulations performed as part of the study completely neglected the effect of damage on the material's elastic and plastic behaviour and the effects of strain rate and temperature-dependent material properties. The developed FE model was used to simulate residual sheet stresses and deformation, though. Belamri et al. [6] and Saanouni et al. [7] coupled Continuum Damage Mechanics with an FE model describing elasto-plastic behaviour to numerically simulate the guillotining of a metallic sheet. An implicit Newton-Raphson scheme, together with a dynamic explicit resolution strategy, was used to analyse the effects of sheet thickness, knife wear, tool deformability, and knife shape on the state of stress in the sheet.

An analysis of the current literature suggests that the main difficulty in modelling guillotining is that only a limited number of FEM models are currently capable of describing the complete shearing process, including the complete separation of the material parts through ductile fracturing. A 3D model describing the primary physical phenomena and characterising the mechanical behaviour of the metal sheet is required to numerically simulate this process using finite element analysis. If 3D modelling used the updated Lagrangian formulation, a FEM that considered process nonlinearity (geometrical, physical, and thermal), large deformations, strain rate, friction and nonlinear material characteristics could be used to analyse the thermo-visco-plastic flow of the material and its stress and strain fields at any time during the guillotining process, successfully numerically reproducing the operation.

In this paper, the guillotining process is considered an initial and boundary value problem with geometrical, physical and thermal nonlinearity and with only partial knowledge of the boundary conditions. The boundary conditions in the tool-sheet contact zones are not known. The paper focuses on the development of a methodology to study the phenomena that occur during and after the cutting process (e.g., the change from a steady state to an unsteady state, sheet deformation, stress and strain states and the sheared edge's characteristic features). Physical and mathematical models of the guillotining process and a new thermo-elastic/thermo-visco-plastic material model are elaborated. The updated Lagrange description is used to describe nonlinear phenomena on a typical incremental step using a stepwise and co-rotational coordinate system. The strain and strain rate states are described using Green-Lagrange strain and strain rate tensors, respectively, and are nonlinear dependences without any linearisation. The procedure is implemented in an application created by the author using ANSYS/LS-DYNA program and the finite element method. The study presents sample simulations and experimentally verifies and analyses the impact of various process conditions on the material's displacements, stresses, strains, and quality of the final product.

## 2. Thermo-elastic and thermo-visco-plastic material model

The goal of this section is to present a material model that considers the combined effects of thermo-elasticity (in the reversible zone) and thermo-visco-plasticity (in the non-reversible zone). The model accounts for the strain, strain rate and material temperature histories. The formulation of the model assumes that the typical small incremental components  $\Delta\varepsilon_{ij}$  of the strain tensor  $\mathbf{T}_{\Delta\varepsilon}$  can be expressed as the sum of the thermo-elastic  $\Delta\varepsilon_{ij}^{(TE)}$ , visco-plastic  $\Delta\varepsilon_{ij}^{(VP)}$  and thermal  $\Delta\varepsilon_{ij}^{(TH)}$  incremental strains:

$$\Delta\varepsilon_{ij} = \Delta\varepsilon_{ij}^{(TE)} + \Delta\varepsilon_{ij}^{(VP)} + \Delta\varepsilon_{ij}^{(TH)}, \quad (1)$$

where  $\Delta\varepsilon_{ij}$ ,  $\Delta\varepsilon_{ij}^{(TE)}$ ,  $\Delta\varepsilon_{ij}^{(VP)}$  and  $\Delta\varepsilon_{ij}^{(TH)}$  are the incremental components of the total, thermo-elastic, visco-plastic and thermal strain tensors, respectively.

The constitutive law for an isotropic, thermo-elastic material with a temperature-dependent module is:

$$\Delta\sigma_{ij} = C_{ijkl}^{(TE)} \left( \Delta\varepsilon_{kl} - \Delta\varepsilon_{kl}^{(VP)} - \Delta\varepsilon_{kl}^{(TH)} \right) + \Delta C_{ijkl}^{(TE)} \varepsilon_{kl}^{(E)}, \quad (2)$$

where  $\Delta\sigma_{ij}$  are the incremental components of the second Piola-Kirchhoff stress,  $\Delta\varepsilon_{ij}$  are the incremental components of the Green-Lagrange strain tensor,  $C_{ijkl}^{(TE)}(T) = \lambda(T)\delta_{ij}\delta_{kl} + \mu(T)(\delta_{ik}\delta_{jl} + \delta_{il}\delta_{jk})$  is the component of the temperature-dependent elastic constitutive tensor,  $\Delta C_{ijkl}^{(TE)}(\Delta T) = \frac{\partial C_{ijkl}^{(TE)}(T)}{\partial T} \Delta T$  are its increments,

$$\lambda(T) = \frac{E(T) \nu(T)}{[1 + \nu(T)] [1 - 2\nu(T)]}, \quad \mu(T) = \frac{E(T)}{2[1 + \nu(T)]}, \quad E(T)$$

and  $\nu(T)$  are the temperature-dependent Young's modulus and Poisson's ratio, respectively,  $\delta_{ij}$  is the Kronecker delta and  $\varepsilon_{kl}^{(E)}$  are the accumulated components of the elastic strain tensor at time  $t$ . The components of the thermal increment strain tensor are calculated from the equation:

$$\Delta\varepsilon_{ij}^{(TH)} \cong \alpha_m(T) \Delta T \delta_{ij}, \quad (3)$$

where  $\alpha_m$  is the mean coefficient of thermal expansion. The visco-plastic incremental strain is defined as [8]:

$$\Delta\varepsilon_{ij}^{(VP)} = \Delta\lambda \frac{\partial F}{\partial \tilde{S}_{ij}}, \quad (4)$$

where  $\Delta\lambda$  is the positive scalar variable or Lagrange's coefficient and  $\tilde{S}_{ij} = S_{ij} - \alpha_{ij}$  is the component of the reduced stress deviator  $\tilde{\mathbf{D}}_{\sigma}$ .

The calculation of  $\Delta\lambda$  requires that a hardening rule be selected. A hardening rule describes the change in the yield surface with continuing plastic deformation. For mixed hardening and an isotropic body, the rule is defined by:

$$\Delta\lambda = \frac{\tilde{S}_{ij} C_{ijkl}^{(TE)} \left( \Delta\varepsilon_{kl}^{(TE)} + \Delta\varepsilon_{kl}^{(VP)} \right) + \tilde{S}_{ij} \Delta C_{ijkl}^{(TE)} \varepsilon_{kl}^{(E)} - A}{\tilde{S}_{ij} C_{ijkl}^{(TE)} \tilde{S}_{kl} + \frac{2}{3} \sigma_Y^2 \left( \tilde{C} + \frac{2}{3} E_T \right)}, \quad (5)$$

where:

$$A = \frac{2}{3} \left[ \sigma_Y \left( \varepsilon_i^{(VP)}, \dot{\varepsilon}_i^{(VP)}, T \right) \right] \left( \dot{E}_T \Delta\varepsilon_i^{(VP)} + T_T \Delta T \right) \quad (6)$$

is the positive scalar variable,  $tg\alpha = E_T(T) = \frac{\partial \sigma_Y}{\partial \varepsilon_i^{(VP)}}$  is

the hardening modulus at  $T$ ,  $tg\beta = \dot{E}_T = \frac{\partial \sigma_Y}{\partial \dot{\varepsilon}_i^{(VP)}}$  is the

change in temporary yield stress with a change in intensity strain rate,  $tg\gamma = T_T = \frac{\partial \sigma_Y}{\partial T}$  is the change of temporary yield

stress with a change in temperature,

$\tilde{C}(T) = \frac{2}{3} \frac{E(T) E_T(T)}{E(T) - E_T(T)}$  is the kinematic hardening param-

eter and  $E$  is Young's modulus at temperature  $T$ . To further evaluate the above expression for  $\Delta\lambda$ , it is necessary to obtain the partial derivatives  $\partial \sigma_Y / \partial \varepsilon_i^{(VP)}$ ,  $\partial \sigma_Y / \partial \dot{\varepsilon}_i^{(VP)}$  and  $\partial \sigma_Y / \partial T$ . It is assumed that a relationship between  $\sigma_Y$ ,  $\varepsilon_i^{(VP)}$ ,  $\dot{\varepsilon}_i^{(VP)}$  and  $T$  can be derived from the data obtained in a series of tensile tests at different temperatures and strain rates using virgin material specimens.

Substituting Eq. (5) into Eq. (4) and using  $\partial F / \partial \tilde{S}_{ij} = \tilde{S}_{ij}$ , we obtain:

$$\Delta\varepsilon_{ij}^{(VP)} = \tilde{S}_{ij}^{**} \Delta\varepsilon_{ij} + \Delta\varepsilon_{ij}^{**}, \quad (7)$$

where:

$$\tilde{S}^{**} = \tilde{S}_{ij}^* C_{ijmn}^{(TE)} \tilde{S}_{mn} \quad (8)$$

is a positive scalar variable,

$$\Delta \varepsilon_{ij}^{**} = \tilde{S}_{ij}^* \left( -C_{ijmn}^{(TE)} \tilde{S}_{mn} \alpha_m \Delta T \delta_{ij} + \tilde{S}_{mn} \Delta C_{mkl}^{(TE)} \varepsilon_{kl}^{(E)} - A \right) \quad (9)$$

is the component of an incremental strain tensor, and:

$$\tilde{S}_{ij}^* = \frac{\tilde{S}_{ij}}{\tilde{S}_{ij} C_{ijkl}^{(TE)} \tilde{S}_{kl} + \frac{2}{3} \sigma_Y^2 \left( \tilde{C} + \frac{2}{3} E_T \right)} \quad (10)$$

is the component of a stress tensor.

Substituting Eqs. (3) and (7) into Eq. (2), we obtain the constitutive equation of mixed hardening for an isotropic material that includes the combined effects of thermo-elasticity and thermo-visco-plasticity:

$$\begin{aligned} \Delta \sigma_{ij} &= C_{ijkl}^{(TE)} (1 - \tilde{S}^{**}) \Delta \varepsilon_{kl} - C_{ijkl}^{(TE)} (\Delta \varepsilon_{kl}^{**} + \alpha_m \Delta T \delta_{kl}) + \\ &+ \Delta C_{ijkl}^{(TE)} \varepsilon_{kl}^{(E)} = C_{ijkl}^{(TE)*} \Delta \varepsilon_{kl} + \Delta \sigma_{ij}^{**}, \end{aligned} \quad (11)$$

where:

$$\left. \begin{aligned} C_{ijkl}^{(TE)*} &= C_{ijkl}^{(TE)} (1 - \tilde{S}^{**}), \\ \Delta \sigma_{ij}^{**} &= -C_{ijkl}^{(TE)} (\Delta \varepsilon_{kl}^{**} + \alpha_m \Delta T \delta_{kl}) + \Delta C_{ijkl}^{(TE)} \varepsilon_{kl}^{(E)}. \end{aligned} \right\} \quad (12)$$

The constitutive model Eq. (11) is used for practical engineering analysis. In the next section, this model is used for the variational formulation of a nonlinear equation of motion for the guillotining operation.

### 3. Variational formulation equation of motion

In this section, we develop an equation of motion for a three-dimensional body in the global Cartesian coordinates  $\{z\}$  and the updated Lagrange incremental formulation. Variational methods are used in continuum mechanics to formulate the equations of motion [8]. However, there is no method of accounting for the incremental formulation. The use of the variational method to formulate the equation of motion for a typical incremental step in nonlinear problems in the technological processes was proposed by Kukielka [9, 10]. In this paper, this method is used to model the guillotining process.

Assuming that a numerical solution has been obtained at discrete time points  $\Delta t, 2\Delta t, \dots$ , the solution for  $t + \Delta t$  is desired. In this case, a functional increment is formulated for incremental displacement  $\Delta \mathbf{R}(\Delta \dot{u}_i, \Delta \dot{u}_i, \Delta \ddot{u}_i) = \Delta \mathbf{F} \cdot$ , where  $\Delta u_i, \Delta \dot{u}_i, \Delta \ddot{u}_i$  are the incremental components of the displacement, velocity and acceleration vectors, respectively. Using the conditions for functional  $\Delta \mathbf{F}(\cdot)$  being stationary [9]:

$$\delta[\Delta \mathbf{F}(\cdot)] = \frac{\partial[\Delta \mathbf{F}(\cdot)]}{\partial(\Delta u_i)} \delta(\Delta u_i) = \frac{\partial[\Delta \mathbf{F}(\cdot)]}{\partial(\Delta u_i)} \Delta \underline{u}_i, \quad (13)$$

where the underline  $(\underline{\cdot})$  denotes ‘‘variation in’’, and we because  $\Delta u_i$  is the only variable, we obtain:

$$\begin{aligned} \delta[\Delta \mathbf{F}(\cdot)] &= \int_V \rho (\ddot{u}_i + \Delta \ddot{u}_i) \Delta \underline{u}_i dV + \alpha \int_V \rho \Delta \dot{u}_i \Delta \underline{u}_i dV - \\ &- 2\omega \int_V \rho \Delta \dot{u}_i \Omega_{ij} \Delta \underline{u}_j dV + \frac{1}{2} \beta \int_V \Delta \dot{\varepsilon}_{ij} C_{ijkl}^{(TE)} \Delta \underline{\varepsilon}_{kl} dV + \\ &+ \frac{1}{2} \beta \int_V \Delta \dot{\varepsilon}_{ij} C_{ijkl}^{(TE)} \Delta \bar{\varepsilon}_{kl} dV + \frac{1}{2} \beta \int_V \Delta \dot{\varepsilon}_{ij} C_{ijkl}^{(TE)} \Delta \tilde{\varepsilon}_{kl} dV + \\ &+ \frac{1}{2} \beta \int_V \Delta \dot{\varepsilon}_{ij} C_{ijkl}^{(TE)} \Delta \bar{\varepsilon}_{kl} dV + \frac{1}{2} \beta \int_V \Delta \dot{\varepsilon}_{ij} C_{ijkl}^{(TE)} \Delta \tilde{\varepsilon}_{kl} dV + \\ &+ \frac{1}{2} \beta \int_V \Delta \dot{\varepsilon}_{ij} C_{ijkl}^{(TE)} \Delta \bar{\varepsilon}_{kl} dV + \frac{1}{2} \beta \int_V \Delta \dot{\varepsilon}_{ij} C_{ijkl}^{(TE)} \Delta \tilde{\varepsilon}_{kl} dV + \\ &+ \frac{1}{2} \beta \int_V \Delta \dot{\varepsilon}_{ij} C_{ijkl}^{(TE)} \Delta \bar{\varepsilon}_{kl} dV + \int_V \Delta \dot{\varepsilon}_{ij} C_{ijkl}^{(TE)*} \Delta \tilde{\varepsilon}_{kl} dV + \\ &+ \int_V \Delta \tilde{\varepsilon}_{ij} C_{ijkl}^{(TE)*} \Delta \bar{\varepsilon}_{kl} dV + \int_V \Delta \tilde{\varepsilon}_{ij} C_{ijkl}^{(TE)*} \Delta \tilde{\varepsilon}_{kl} dV + \\ &+ \int_V \Delta \bar{\varepsilon}_{ij} C_{ijkl}^{(TE)*} \Delta \bar{\varepsilon}_{kl} dV + \frac{1}{2} \int_V (T_{ij} + \Delta \sigma_{ij}^{**}) \Delta \tilde{\varepsilon}_{ij} dV + \\ &+ \frac{1}{2} \int_V (T_{ij} + \Delta \sigma_{ij}^{**}) \Delta \bar{\varepsilon}_{ij} dV - \omega^2 \int_V \rho \Delta u_i \Omega_{ij} \Omega_{ij} \Delta \underline{u}_i dV - \\ &- \omega^2 \int_V \rho r_i \Omega_{ij} \Omega_{ij} \Delta \underline{u}_i dV - \int_V \rho (f_i + \Delta f_i) \Delta \underline{u}_i dV - \\ &- \int_{\Sigma_k} (\hat{p}_i + \Delta \hat{p}_i) \Delta \underline{u}_i d \Sigma_k = 0, \end{aligned} \quad (14)$$

where  $T_{ij}$  is the component of Cauchy’s stress tensor,  $\alpha$  and  $\beta$  are constants (to be determined from two given damping ratios that correspond to two unequal frequencies of vibration),  $\Delta \dot{\varepsilon}_{ij}$  and  $\Delta \tilde{\varepsilon}_{ij}$  are the linear and nonlinear incremental components of the Green-Lagrange strain rate tensor, respectively. ( $\Delta \dot{\varepsilon}_{ij} = \partial \Delta \bar{\varepsilon}_{ij} / \partial t$ ;  $\Delta \tilde{\varepsilon}_{ij} = \partial \Delta \tilde{\varepsilon}_{ij} / \partial t$ ),  $\Delta \bar{\varepsilon}_{ij} = (\Delta u_{i,j} + \Delta u_{j,i} + u_{i,i} \Delta u_{i,j} + \Delta u_{i,i} u_{i,j}) / 2$  and formula  $\Delta \tilde{\varepsilon}_{ij} = (\Delta u_{i,k} \Delta u_{j,k}) / 2$  are the linear and nonlinear incremental components of the Green-Lagrange’s strain tensor, respectively.  $\rho(T)$  is the temperature-dependent mass density at time  $t$  and  $\varepsilon_{ij}$  are the accumulated components of the total strain tensors at time  $t$  (depending on the history of deformation and temperature).  $f_i, \Delta f_i$  are the components of the internal force and incremental force vectors, respectively,  $\hat{p}_i, \Delta \hat{p}_i$  are the components of the externally applied surface force and surface incremental force vectors in the contact body zones, respectively, and  $\Omega_{ij}$  are the components of the gyro tensor. However, in the typical updated Lagrange formulation  $\Delta \bar{\varepsilon}_{ij} = (\Delta u_{i,j} + \Delta u_{j,i}) / 2$ . The integrations are performed over the volume  $V$  and surface  $\Sigma$  of the body, and Eq. (14) provides the basis for the finite element discretisation required to obtain a solution.

### 4. Numerical analysis algorithm

Assuming that the temporary step time  $\Delta t$  is very

small, it is possible to remove the incremental stiffness matrix ( $\Delta \mathbf{K} \approx 0$ ) and internal incremental force vector ( $\Delta \mathbf{F} \approx 0$ ). Then, using the principle of incremental decomposition, approximating the  $\dot{\mathbf{r}}$  and  $\ddot{\mathbf{r}}$  in terms of  $\mathbf{r}$  in Eq. (14) using the central difference method (DEM), and using the following approximate [11]:

$${}^t\dot{\mathbf{r}} = \frac{1}{2\Delta t}({}^{\tau}\mathbf{r} - {}^{t-\Delta t}\mathbf{r}), \quad {}^t\ddot{\mathbf{r}} = \frac{1}{\Delta t^2}({}^{\tau}\mathbf{r} - 2{}^t\mathbf{r} + {}^{t-\Delta t}\mathbf{r}), \quad (15)$$

we obtain the solution of  ${}^t\mathbf{r}$  :

$$\tilde{\mathbf{M}} {}^t\mathbf{r} = \tilde{\mathbf{Q}}, \quad (16)$$

where  $\tilde{\mathbf{M}}$  is the effective mass matrix and  $\tilde{\mathbf{Q}}$  the effective load vector:

$$\tilde{\mathbf{M}} = a_0\mathbf{M} + a_1\mathbf{C}, \quad (17)$$

$$\tilde{\mathbf{Q}} = \mathbf{F} + \mathbf{R} + a_0\mathbf{M}(2{}^t\mathbf{r} - {}^{t-\Delta t}\mathbf{r}) + a_1\mathbf{C} {}^{t-\Delta t}\mathbf{r}, \quad (18)$$

with the integration constants:  $a_0 = 1/(\Delta t^2)$ ,  $a_1 = 1/(2\Delta t)$ .

#### 4.1. Step-by-step solution using the Central Difference Method

In this section, the Central Difference Method [11, 12] is adopted to solve Eq. (16) with initial and boundary conditions.

Initial calculations:

1. Form mass  $\mathbf{M}$  and damping  $\mathbf{C}$  matrices.

2. Initialise  ${}^0\mathbf{r}$ ,  ${}^0\dot{\mathbf{r}}$  and  ${}^0\ddot{\mathbf{r}}$ .

3. Select a time step  $\Delta t < \Delta t_{cr} = T_N / \pi$  and calculate the integration constants  $a_0$  and  $a_1$ .

4. Calculate  ${}^{-\Delta t}\mathbf{r}$ .

5. Form an effective stiffness matrix  $\tilde{\mathbf{M}}$  from Eq. (17).

For each time step:

1. Calculate the effective load vector  $\tilde{\mathbf{Q}}$  from Eq. (18).

2. Partitioning the equilibrium equation for two blocks, write the problem in the form:

$$\begin{bmatrix} \tilde{\mathbf{M}}_{11}^{n \times n} & \tilde{\mathbf{M}}_{12}^{n \times w} \\ \tilde{\mathbf{M}}_{21}^{w \times n} & \tilde{\mathbf{M}}_{22}^{w \times w} \end{bmatrix} \begin{Bmatrix} {}^{\tau}\mathbf{r}_1^{n \times 1} \\ {}^{\tau}\mathbf{r}_2^{w \times 1} \end{Bmatrix} = \begin{Bmatrix} \tilde{\mathbf{Q}}_1^{n \times 1} \\ \tilde{\mathbf{Q}}_2^{w \times 1} \end{Bmatrix},$$

where vectors  ${}^{\tau}\mathbf{r}_2^{w \times 1}$ ,  $\tilde{\mathbf{Q}}_1^{n \times 1}$  are known and vectors  ${}^{\tau}\mathbf{r}_1^{n \times 1}$ ,  $\tilde{\mathbf{Q}}_2^{w \times 1}$  are unknown.

3. Solve for the displacement vector  ${}^{\tau}\mathbf{r}_1^{n \times 1}$ :

$${}^{\tau}\mathbf{r}_1^{n \times 1} = (\tilde{\mathbf{M}}_{11}^{n \times n})^{-1} \cdot [\tilde{\mathbf{Q}}_1 - \tilde{\mathbf{M}}_{12}^{n \times w} {}^{\tau}\mathbf{r}_2^{w \times 1}],$$

4. Substitute vector  ${}^{\tau}\mathbf{r}_1^{n \times 1}$  into the equation:

$$\tilde{\mathbf{Q}}_2^{w \times 1} = \tilde{\mathbf{M}}_{21}^{w \times n} {}^{\tau}\mathbf{r}_1^{n \times 1} + \tilde{\mathbf{M}}_{22}^{w \times w} {}^{\tau}\mathbf{r}_2^{w \times 1},$$

and solve to obtain the load vector  $\tilde{\mathbf{Q}}_2^{w \times 1}$  in the tool-object contact zone.

5. Calculate the vectors  ${}^t\dot{\mathbf{r}}$  and  ${}^t\ddot{\mathbf{r}}$  from Eq. (15).

## 5. Sample solution

A three-dimensional finite element model of guillotining is presented in Figs. 2 and 3. Numerical calculations are performed for the 3D state of strain and 3D state of stress in this model. It is assumed that the cutting process takes place under a constant temperature ( $\Delta T = 0$ ). The models in Eqs. (11) and (14) then reduce to the elastic (in the reversible zone) and visco-plastic (in the non-reversible zone) strains. Moreover:  $\lambda(T) = \lambda$ ,  $\mu(T) = \mu$ ,  $\rho(T) = \rho$ ,  $\Delta \varepsilon_{ij}^{(TH)} = 0$ ,  $\Delta C_{ijkl}^{(TE)}(\Delta T) = 0$ ,  $C_{ijkl}^{(TE)} = C_{ijkl}^{(E)}$  and  $\Delta \sigma_{ij}^{**} = -C_{ijkl}^{(TE)} \Delta \varepsilon_{kl}^{**}$ . 1018 steel is used as the material to be cut in the numerical and experimental studies, and an element with a length of  $l = 50$  mm, width of  $w_i = 40$  mm and thickness of  $t = 1$  mm is analysed. A velocity of  $v = 200$  mm/s is applied to the upper knife in the  $y$  direction. The objects are meshed with an 8-node Solid164 element type with reduced integration and hourglass control, and the mapped mesh is generated with various sheet densities (Fig. 3). The finite element model of the sheet uses 2760000 elements, that of the upper knife uses 38170 and that of the lower knife uses 24300. The contact between ideally rigid tools and the deformable sheet metal is described using Coulomb's friction model, and constant coefficients of static friction  $\mu_s = 0.08$  and kinetic friction  $\mu_d = 0.009$  are accepted. The LS-DYNA contact model "automatic surface to surface" is used in the analysis.

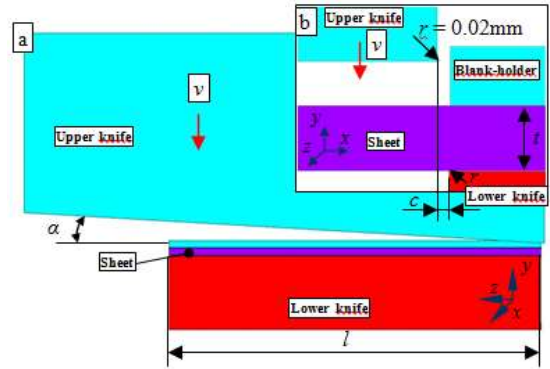


Fig. 2 Computer model of the guillotining process: a) side view and b) front view

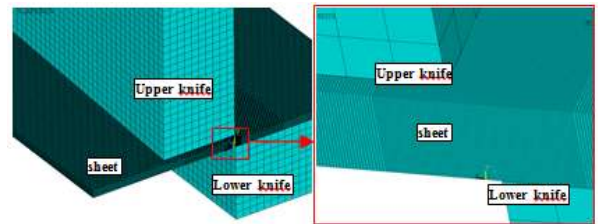


Fig. 3 Initial mesh of the guillotining process

The tools (knives) are considered rigid bodies, but the sheet is modelled as the isotropic, elastic/visco-plastic material with nonlinear hardening, the temporary yield stress of which is described with the aid of the

Cowper-Symonds model [13]:

$$\sigma_Y = \left[ 1 + \left( \dot{\varepsilon}_i^{(P)} / C \right)^m \right] \left( \sigma_0 + \beta E_p \varepsilon_i^{(P)} \right), \quad (19)$$

where  $\beta$  is the plastic strain hardening parameter,  $\sigma_0$  is the initial, static yield point,  $\dot{\varepsilon}_i^{(P)}$  is the plastic strain rate intensity,  $C$  is the material parameter defining the effect of the plastic strain rate intensity,  $m = 1/n$  is a material constant defining its sensitivity to the plastic strain rate,  $\varepsilon_i^{(P)}$  is the plastic strain intensity and  $E_p = \frac{E_T E}{E - E_T}$  is the material parameter depending on the modulus of plastic strain hardening and Young's modulus  $E$ .

The Cowper-Symonds material deformation model is frequently used to perform simulations of dynamic processes using the FE method. Although the majority of material constants are determined using a classical tension test, problems are associated with the determination of the Cowper-Symonds constants  $C$  and  $n$ . In a previous report [13], we established the values of Cowper-Symonds constants at different deformation rates. The values of the constants for the 1018 steel are taken as follows in this study:  $C = 40 \text{ s}^{-1}$  and  $n = 5$ , while  $\rho = 7800 \text{ kg/m}^3$ ,  $\sigma_0 = 310 \text{ MPa}$ ,  $E = 210 \text{ GPa}$ ,  $\nu = 0.27$ ,  $E_T = 763 \text{ MPa}$ , and  $\beta = 1$ .

To simulate the crack initiation and propagation in the material, we use a new constitutive model proposed by Xue and Wierzbicki [14]. The model covers the full range of plasticity until the onset of fracture. It is understood that the fracture initiation in uncracked solids is the ultimate result of a complex damage accumulation process induced by plastic deformations. Fracture can be predicted for complex loading paths that are not limited to restricted loading in which the pressure is constant. The model also incorporates the coupling between the damage and the strain hardening function. We determined the model constants experimentally and presented them in [15].

In the next section, we illustrate the present solution procedure's capability to reproduce the effects of process technological parameters such as the rake angle and clearance on the quality of the sheet cutting process. The computer simulations and experiments are executed for different rake angle values of  $\alpha_1 = 1^\circ$ ,  $\alpha_2 = 3^\circ$ ,  $\alpha_3 = 6^\circ$ , and  $\alpha_4 = 12^\circ$  and clearance values of  $c_1 = 0.01 \text{ mm}$ ,  $c_2 = 0.04 \text{ mm}$ ,  $c_3 = 0.1 \text{ mm}$ ,  $c_4 = 0.15 \text{ mm}$  and  $c_5 = 0.2 \text{ mm}$ .

## 6. Results and discussion

### 6.1. Guillotining force

Fig. 4 shows the evolution of the guillotining force compared to the upper knife penetration. In guillotining ( $\alpha > 0^\circ$ ), only a portion of the sheet is cut at one time. Therefore, the stationary cutting force  $F_{sta}$  is independent of the cut length. The cutting force depends mainly on the rake angle and sheet thickness for a given material, and an increasing rake angle leads to lower forces  $F_{sta}$  over larger displacements. The cutting operation requires only a small knife displacement when  $\alpha = 1^\circ$  is used. The initiation of the macroscopic crack (cutting operation) starts at approximately  $w_{sta} = 0.25 \text{ mm}$  for  $\alpha = 1^\circ$  (Fig. 4) and propagates in a

stationary manner until the final fracture of the sheet observed at  $w_{fra} = 0.58 \text{ mm}$ , which corresponds to the end of the cutting operation. The more  $\alpha$  increases, the larger the steady state stage of the process becomes. When  $\alpha = 12^\circ$ , the steady state extends from  $w_{sta} = 0.4 \text{ mm}$  to  $w_{fra} = 10.5 \text{ mm}$ . From our numerical and experimental results, we find that a rake angle of  $\alpha = 3^\circ$  provides a good compromise in terms of the mechanical work (or energy) needed to achieve the cutting operation on the sheet using this type of knife. In fact, the rake angle of  $\alpha = 3^\circ$  requires 17% less energy than  $\alpha = 1^\circ$ , while a rake angle of  $\alpha = 6^\circ$  requires 29% more energy. The results obtained for this case show that the cutting operation ends when the upper knife penetrates sheet by approximately  $w = 3.5 \text{ mm}$ . The values of the forces obtained from the numerical calculation show differences of less than 10% from the experimental results. For example, the maximum force obtained from a simulation when  $\alpha = 1^\circ$  is 2.72 kN (versus 2.94 kN obtained experimentally), and that when  $\alpha = 12^\circ$  is 1.46 kN (versus 1.62 kN).

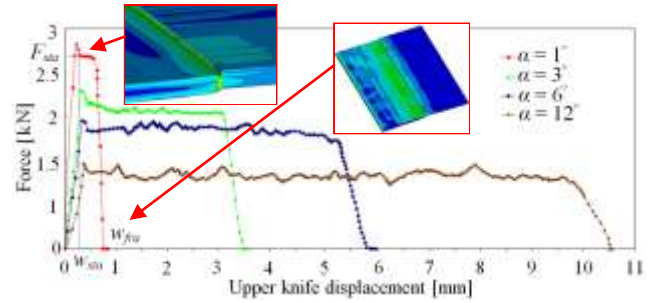


Fig. 4 Evolution of the guillotining force versus upper knife displacement for the analysed rake angles ( $c = 0.1 \text{ mm}$ )

### 6.2. Effect of the rake angle ( $\alpha$ ) on stress states and sheet deformation

Fig. 5 presents the stress component in the  $z$ -direction  $\sigma_{zz}$  inside the sheet for different rake angles.

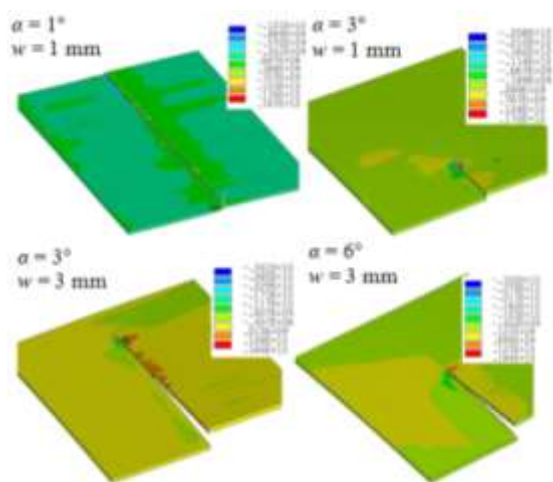


Fig. 5  $\sigma_{zz}$ , Pa and evolution of the crack length based on the upper knife penetration  $w$  (clearance  $c = 0.1 \text{ mm}$ )

It can be seen that the stresses in the  $z$ -direction form bending moments. The stress is positive at the top and negative at the bottom of the sheet, or vice versa, and the sheet is bent twice to conform to the knife configuration. These stresses are typical for guillotining and are not

found in orthogonal shearing. The bending stresses increase with increasing rake angle as the sheet is bent over a larger angle. Both the values and distribution of stresses change for increasing rake angles because the process zone becomes shorter for larger rake angles.

Fig. 6 shows the displacement of the sheet after processing in the y-direction for rake angles  $\alpha = 1^\circ$ ,  $\alpha = 6^\circ$  and  $\alpha = 12^\circ$  with a constant clearance value of  $c = 0.1$  mm.

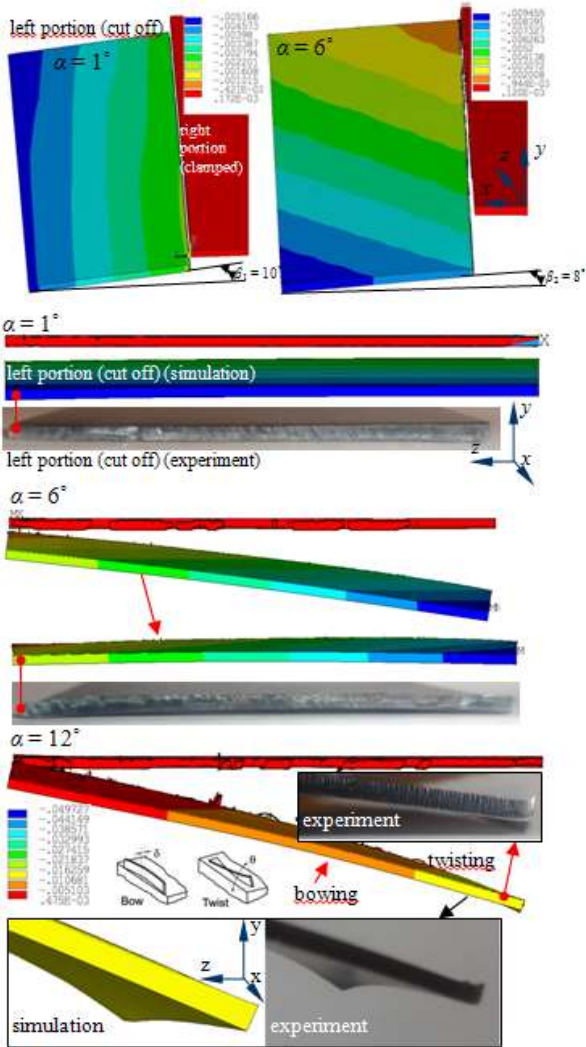


Fig. 6 y-component of the displacement, m and sample comparison of predicted sheet deformations with experimental data

The deformations of these sheets are non-symmetrical at rake angles of  $\alpha = 1^\circ$  and  $\alpha = 6^\circ$ . The bending of the sheet during guillotining is restricted by the other cross-sections in different stages of the process. The left portion of the sheet that is not clamped bends away from the upper knife by approximately  $\beta_1 = 10^\circ$  for a rake angle of  $\alpha = 1^\circ$  and by approximately  $\beta_2 = 8^\circ$  for a rake angle of  $\alpha = 6^\circ$ . The shearing deformation during guillotining is accompanied by a bending deformation, and these deformations influence each other, which leads to the development of shape defects such as twisting and bowing. The maximum displacement when  $\alpha = 1^\circ$  occurs along the left edge of the cut-off portion and measures approximately 5 mm. This displacement value decreases with the width of the sheet to a value of 2 mm in the shearing region, and changes with the length of the sheet when  $\alpha = 6^\circ$ . The mini-

um displacement value (2 mm) occurs in the right corner at the end of the sheet and the maximum value (9.5 mm) occurs in the left corner at the front of the sheet. Three characteristic displacement areas are observed when  $\alpha = 12^\circ$ . The maximum displacement obtained is approximately 14.7 mm. The contours of the sheets from the experiments are measured after the process and compared with the simulation results. The good agreement between these results indicates that the FEM simulations employed in this work can give accurate predictions of sheet deformations.

### 6.3. Effect of the rake angle ( $\alpha$ ) and clearance ( $c$ ) on the quality of the sheared edge

The exemplary results obtained from the numerical calculations for equivalent stress distribution and sheared edge contours after the guillotining process are illustrated in Fig. 8. The area values (Fig. 7) are measured from the simulations and experiments at different locations over the cut edge in the z-direction, averaged and presented in Fig. 9. The results are in good agreement with those obtained from the experiments, with an approximate error margin of 11%. In industrial practice, one must attempt to obtain the longest possible share of fractured area with the smallest possible share of fractured area, draw-in/roll-over, and burr height.

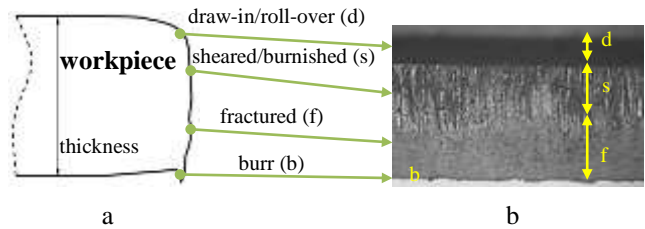


Fig. 7 a) Typical shear profile (cross-sectional view) of the sheared edge with marked zones, and b) view of the sample sheared edge obtained experimentally (front view)

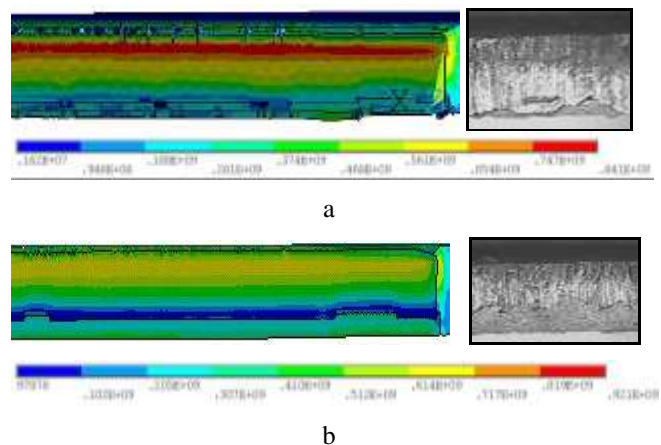


Fig. 8 Characteristic features of the selected sheared edges viewed by optical microscopy and predicted by FE simulations (equivalent stress distribution, Pa) at a)  $\alpha = 1^\circ$ ,  $c = 0.01$  mm and b)  $\alpha = 3^\circ$ ,  $c = 0.04$  mm

The results show that the rake angle and clearance values have a major influence on the quality of the sheared edge. The value of the draw-in/roll-over area depends mainly on the clearance value (Fig. 9, a). Increasing the clearance

from  $c = 0.01$  mm to  $c = 0.1$  mm significantly reduces this area at the analysed rake angles. As the rake angle increases, the sheared/burnished area decreases (Fig. 9, b), and the largest area values are obtained when the clearances are set to the middle range (8-10% of the sheet thickness). The fractured area depends strongly on the rake angle value when small clearances are used (1-5% of the sheet thickness), but increases areas the rake angle increases (Fig. 9, c).

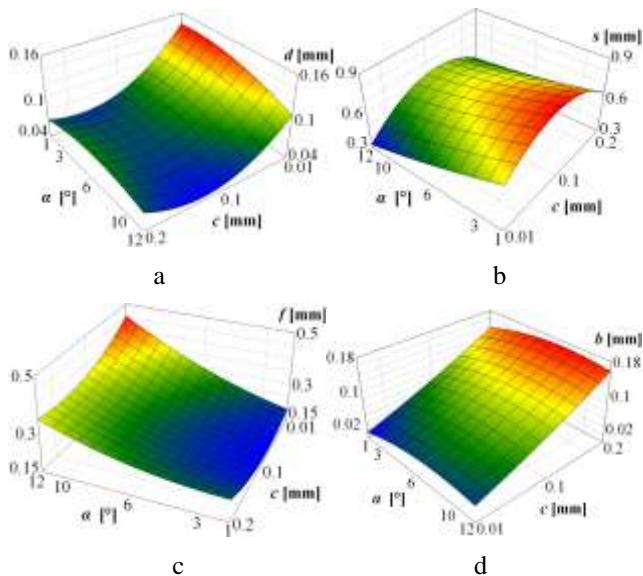


Fig. 9 Influence of rake angle and clearance on: a) draw-in/roll-over; b) sheared/burnished; c) fractured and d) burr area

It is evident from these analyses that changing the clearance significantly influences the height of the burrs (Fig. 9, d). Increasing the clearance increased the burr height for the rake angles under analysis. The maximum burr height was found using a rake angle of  $\alpha = 6^\circ$  and clearance of  $c = 0.2$  mm. Reducing the clearance to  $c = 0.01$  mm significantly reduced the average burr height at this rake angle. From the results obtained in this study, it can be seen that the fracture process because less steady as the rake angle increases, and progresses in a non-uniform manner. The transition of the material fracture from the “shear mode” to the “shear and tear mode” (Fig. 10) is observed for higher rake angles ( $\alpha = 6^\circ$ , and  $\alpha = 12^\circ$ ) during guillotining.

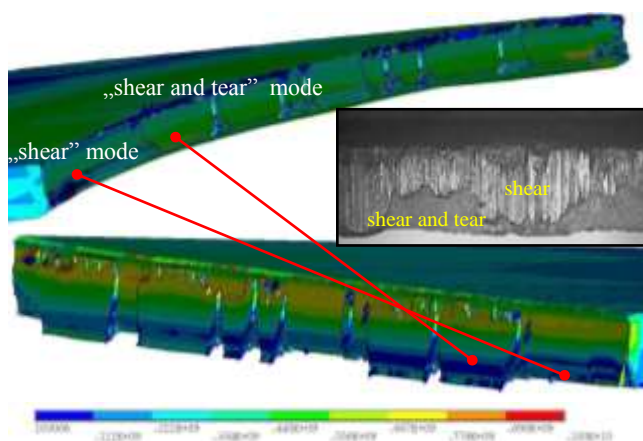


Fig. 10 Transition of the material fracture mode from the “shear” to the “shear and tear” mode ( $\alpha = 6^\circ$ ,  $c = 0.1$  mm) (equivalent stress distribution, Pa)

A dramatic transition of the fracture mode from the “shear mode” to the “shear and tear mode” is also observed in the developed simulations and experiments at certain locations, and the non-uniformity of the two parts’ fractured surfaces at rake angles of  $\alpha = 6^\circ$ , and  $\alpha = 12^\circ$  match perfectly. This result suggests that shearing under such conditions is a three-dimensional, rather than a two-dimensional, problem. The fracture process is unsteady and progresses in a non-uniform manner because of the stress and strain states created by the macroscopic cutting conditions. Switching the mode from a 2D “shear” to a 3D “shear and tear” process requires that the fracture occur in the third dimension. If the localisation zone is sufficiently concentrated, then fractures in the third dimension are not permissible. Additionally, a tensile force component in the x-direction is required for a “tear” to occur, and the angled cutting configuration provides that tensile force.

## 7. Conclusions

The objective of this paper was to present the modelling, analysis and testing of a procedure for analysing the guillotining process. Dynamic and damage effects, thermo-mechanical coupling and contact friction were accounted in the study. The procedure was implemented in an application created by the authors using finite element code in the ANSYS/LS-DYNA program. Their main conclusion is that most trends in the guillotining process are qualitatively well described by the developed model, which analyses the stress and strain states at any moment during the process and identifies the causes of these defects in the metal sheets after processing (deformation, twisting, bowing, and defects on the sheared edge, such as burrs and chips). It is important to apply the required boundary conditions for guillotining, considering the dimensions of the sheet that is being cut. Special attention should be paid to correctly modelling the clamping of the sheet, which also means that the 3D models cannot simply be replaced by 2D approximations.

The simulation results agreed well with experiments in the study, indicating that the model could be used to both design the guillotining process and support the solution of practical problems. Actual investigations concern the simulation of guillotining, in which the knives cannot be considered rigid bodies. Further work is still required to introduce other effects concerning the behaviour of the rolled metal sheets, such as damage-induced anisotropy and spring-back effects.

## References

1. **Domski, J.; Katzer, J.** 2013. Load-deflection characteristic of fibre concrete based on waste ceramic aggregate, Annual Set The Environment Protection 15: 213-230.
2. **Hilditch, T.; Hodgson, P.** 2005. Development of the sheared edge of the trimming of steel and light metal sheet, Part 1, Experimental observations, Journal of Materials Processing Technology 169: 184-191. <http://dx.doi.org/10.1016/j.jmatprotec.2005.02.266>.
3. **Zilinskaite, A.; Ziliukas, A.** 2008. General deformation flow theory, Mechanika 2(70): 11-15.
4. **Wisselink, H.** 2000. Analysis of guillotining and slitting, finite element simulations, Ph.D - Thesis, University of Twente, The Netherlands. <http://doc.utwente.nl/32067/1/t0000015.pdf>.

5. **Wisselink, H.; Hue'ink, J.** 2004. 3D FEM simulation of stationary metal forming processes with applications to slitting and rolling, *Journal of Materials Processing Technology* 148: 328-341.  
<http://dx.doi.org/10.1016/j.jmatprotec.2004.02.036>.
6. **Belamri, N.C.N.; Saanouni, K.; Autesserre, P.** 2006. Residual stresses in 3D sheet metal guillotining using a coupled finite elastoplastic damage model, *Materials Science Forum* 524-525: 89-94.  
<http://dx.doi.org/10.4028/www.scientific.net/MSF.524-525.89>.
7. **Saanouni, K.; Belamri, N.C.N.; Autesserre, P.** 2010. Finite element simulation of 3D sheet metal guillotining using advanced fully coupled elastoplastic-damage constitutive equations, *Finite Elements in Analysis and Design* 46: 535-550.  
<http://dx.doi.org/10.1016/j.finel.2010.02.002>.
8. **Kleiber, M.** 1985. Finite element method in non-linear solid mechanics, IPPT PAN, PWN, Warsaw-Poznan.
9. **Kukielka, L.; Geleta, K.; Kukielka, K.** 2012. Modelling of initial and boundary problems with geometrical and physical nonlinearity and its application in burnishing processes, *Steel Research International, Special Edition, 14th International Conference on Metal Forming*: 1375-1378.  
<http://www.materialsvIEWS.com/metal-forming-2012/>.
10. **Kulakowska, A.; Kukielka, L.** 2008. Numerical analysis and experimental researches of burnishing rolling process with taking into account deviations in the surface asperities outline after previous treatment, *Steel Research International* 2: 42-48.
11. **Bathe, K.J.** 1982. Finite Element Procedures in Engineering Analysis, Prentice-Hall, Englewood Cliffs, New Jersey, 736 p.
12. **Patyk, R.; Kukielka, L.** 2008. Optimization of geometrical parameters of regular triangular asperities of surface put to smooth burnishing, *Steel Research International* 2: 642-647.
13. **Bohdal, L.; Kukielka, L.** 2006. The effect of selected material parameters on the stress and strain states in the process of cutting a sheet plate with circular cutters, *Task Quarterley* 4: 391-400.
14. **Xue, L.; Wierzbicki, T.** 2013. Verification of a new fracture criterion using LS-DYNA, 9th International LS-DYNA Users Conference, *Simulation Technology* 3: 13-22.
15. **Bohdal, L.; Kukielka, L.** 2013. The modeling and numerical analysis of the shearing process with the regard of the geometrical and physical nonlinearity, *Ecological Aspects of Applying New Technologies In Transport*: 131-140.

L. L. Bohdal, L. Kukielka

VARIACINIO IR BAIGTINIŲ ELEMENTŲ METODŲ  
 TAIKYMAS GILJOTINAVIMO PROCESO  
 GEOMETRINIAMS IR FIZIKINIAMS  
 NETIESIŠKUMAMS TIRTI IR MODELIUOTI

Re z i u m ė

Modeliavimas baigtinių elementų metodu padeda kompleksiskai suvokti technologinių procesų ypatumus. Šiame straipsnyje pateikiami variacinis ir baigtinių ele-

mentų metodai giljotininio proceso analizei ir jo netiesiškumų įvertinimui. Sudaryti šio proceso fizinis ir matematinis bei naujas termo-elastinis/termo-klampumo-plastinis modeliai. Skaičiavimai atlikti ANSYS/LS-DYNA paketo pagalba, o modelis parinktas palyginus modeliavimo ir eksperimento rezultatus. Atlikta įvairių proceso sąlygų įtakos analizė įtempimų, deformacijų būviamis ir galutinio produkto kokybei.

L. Bohdal, L. Kukielka

APPLICATION OF VARIATIONAL AND FEM  
 METHODS TO THE MODELLING AND NUMERICAL  
 ANALYSIS OF GUILLOTINING PROCESS FOR  
 GEOMETRICAL AND PHYSICAL NONLINEARITY

S u m m a r y

Finite element modelling provides a great deal of support in understanding technological processes. However, there are few studies of the guillotining process, and those that exist are simplified for use only in the calculation of such processes' steady states. This paper proposes the application of variational and finite element methods for the analysis of guillotining and the nonlinearities of this process. Physical and mathematical models of the process and a new thermo-elastic/thermo-visco-plastic material model are elaborated. The procedure is implemented in the finite element code ANSYS/LS-DYNA and the model is validated comparing the numerical and experimental results. The influence of various process conditions on the strain and stress states and the quality of the final product are analysed. The results lay the groundwork for further study regarding the numerical analysis of spring-back behaviour and the effect of tool elasticity on the quality of the final work piece.

**Keywords:** Guillotining, constitutive laws, modelling, numerical simulation, variational formulation, FEM.

Received Mai 14, 2013

Accepted March 21, 2014